iScience

CellPress
OPEN ACCESS

Article

# Complex magnetism of single-crystalline AlCoCrFeNi nanostructured high-entropy alloy

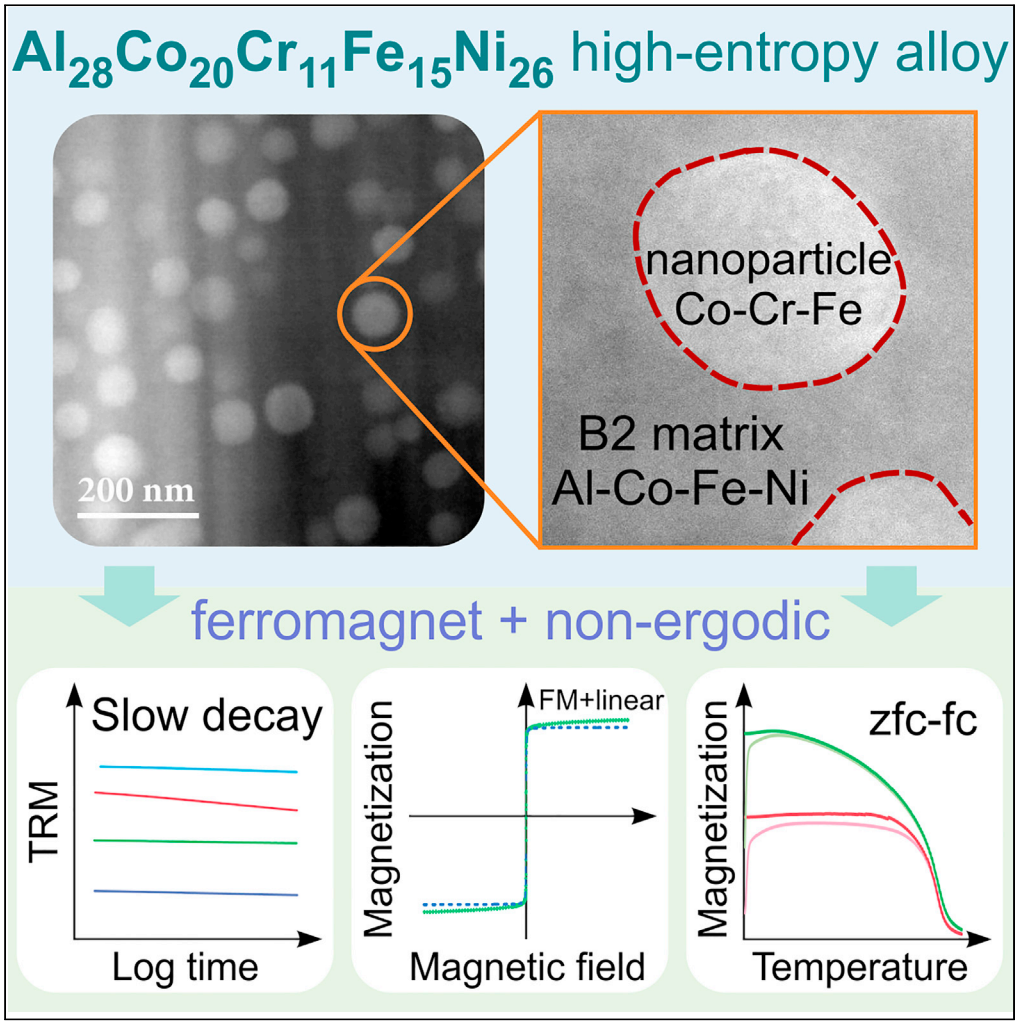


Primož Koželj, Andreja Jelen, Goran Dražić, ..., Anton Meden, Michael Feuerbacher, Janez Dolinšek

m.feuerbacher@fz-juelich.de (M.F.)
jani.dolinsek@ijs.si (J.D.)

## Highlights

Complex magnetism of nanostructured AlCoCrFeNi high-entropy alloy was investigated

The material is composed of a B2 matrix with dispersed spherical A2 nanoparticles

The AlCoFeNi B2 matrix forms a disordered ferromagnetic state with $T_C \approx 390$ K

The CoCrFe nanoparticle cores are asperomagnetic with thin ferromagnetic shells

Koželj et al., iScience 26, 106894
June 16, 2023 
https://doi.org/10.1016/j.isci.2023.106894

iScience

CellPress
OPEN ACCESS

Article

# Complex magnetism of single-crystalline AlCoCrFeNi nanostructured high-entropy alloy

Primož Koželj,[1,2] Andreja Jelen,[1] Goran Dražić,[3] Stanislav Vrtnik,[1] Jože Luzar,[1] Magdalena Wencka,[1,4] Anton Meden,[5] Michael Feuerbacher,[6,*] and Janez Dolinšek[1,2,7,*]

## SUMMARY

**We have investigated magnetism of the $Al_{28}Co_{20}Cr_{11}Fe_{15}Ni_{26}$ single-crystalline high-entropy alloy. The material is nanostructured, composed of a B2 matrix with dispersed spherical-like A2 nanoparticles of average diameter 64 nm. The magnetism was studied from 2 to 400 K via direct-current magnetization, hysteresis curves, alternating-current magnetic susceptibility, and thermoremanent magnetization time decay, to determine the magnetic state that develops in this highly structurally and chemically inhomogeneous material. The results reveal that the Cr-free B2 matrix of composition $Al_{28}Co_{25}Fe_{15}Ni_{32}$ forms a disordered ferromagnetic (FM) state that undergoes an FM transition at $T_C \approx$ 390 K. The Al- and Ni-free A2 nanoparticles of average composition $Co_{19}Cr_{56}Fe_{25}$ adopt a core-shell structure, where the shells of about 2 nm thickness are CoFe enriched. While the shells are FM, the nanoparticle cores are asperomagnetic, classifying into the broad class of spin glasses. Asperomagnetism develops below 15 K and exhibits broken-ergodicity phenomena, typical of magnetically frustrated systems.**

## INTRODUCTION

High-entropy alloys (HEAs) are crystalline solid solutions, composed of five or more different chemical elements in near-equiatomic ratios. Single-phase solid solutions with a random distribution of chemical elements on the lattice, crystallizing on simple lattices like a body-centered cubic (bcc), a face-centered cubic (fcc), and a hexagonal close-packed (hcp), are conveniently denoted as the "first-generation" HEAs.[1] Experimentally, such HEAs have been realized as hcp mixtures of rare earth elements from the heavy half of the lanthanide series (from Gd to Lu, but excluding Yb) and Y[2–8] and the fcc Cantor alloy CoCrFeMnNi.[9] A much larger class of HEAs are the systems containing more than one phase, typically from two to four, but still fewer than the maximum number allowed by the Gibb's phase rule. These "second-generation" HEAs are sometimes denoted as compositionally complex alloys (CCAs),[1] and their multiphase structure frequently results in technologically relevant and tunable physical-mechanical properties like high hardness and strength (due to the precipitation strengthening mechanism), a combination of hardness and ductility (one phase is hard and the other one ductile), and a combination of magnetic softness and zero magnetostriction for supersilent alternating-current applications like a "non-humming" grid transformer.[10] The formation of multiphase structures originates from the interplay between the elements' binary mixing enthalpies, atomic size differences, different electronegativities, and unequal crystal structures of pure elements.[11] The phase separation is sometimes hierarchical, appearing simultaneously on both the micrometer (1–100 μm) and the nanometer (10 to several 100 nm) scales, forming nanostructured material. When at least one dimension is in the nanometer range, materials behave differently from the bulk homogeneous materials and exhibit size-specific physical (magnetic and electrical) properties like superparamagnetism, remanence enhancement, exchange averaging of magnetic anisotropy, giant magnetoresistance, and granular superconductivity.[12] The number of possible nanostructured HEAs is inexhaustible, prompting to search for new multiphase HEAs with unique physical properties introduced by their nanostructure.

An example of an HEA system that decomposes hierarchically into two phases is the Al-Co-Cr-Fe-Ni, where the matrix structure is B2 (a chemically ordered bcc), while the structure of the inclusions is A2 (a randomly chemically disordered bcc).[13–16] The decomposition forms a multi-length-scale micro- and nanostructure,

[1]Jožef Stefan Institute, Jamova 39, SI-1000 Ljubljana, Slovenia

[2]University of Ljubljana, Faculty of Mathematics and Physics, Jadranska 19, SI-1000 Ljubljana, Slovenia

[3]National Institute of Chemistry, Department of Materials Chemistry, Hajdrihova 19, SI-1000 Ljubljana, Slovenia

[4]Institute of Molecular Physics, Polish Academy of Sciences, Smoluchowskiego 17, PL-60-179 Poznań, Poland

[5]University of Ljubljana, Faculty of Chemistry and Chemical Technology, Večna Pot 113, SI-1000 Ljubljana, Slovenia

[6]Ernst Ruska-Centre for Microscopy and Spectroscopy with Electrons, Forschungszentrum Jülich GmbH, 52425 Jülich, Germany

[7]Lead contact

*Correspondence: m.feuerbacher@fz-juelich.de (M.F.), jani.dolinsek@ijs.si (J.D.)

https://doi.org/10.1016/j.isci.2023.106894

with the A2 inclusions sizes ranging from coarse (average size of several μm) to medium scale (from several 10 up to a few 100 nm) to fine scale (<10 nm). The actual decomposition depends sensitively on the concentration of the elements, the method of synthesis, and the thermal annealing conditions. Due to the involvement of magnetic elements Co, Cr, Fe, and Ni, this hierarchically decomposed system is a nanostructured magnetic HEA.

The micro- and nanostructure of the Al-Co-Cr-Fe-Ni system have been studied in detail for polygrain samples of nominal average composition $AlCo_{0.5}Cr_{0.5}FeNi$, prepared by the arc-melting method and annealed at either 600°C or 1000°C,[15,16] and for an as-cast sample of equiatomic composition AlCoCrFeNi, prepared by induction melting.[13] Hierarchically decomposed B2 + A2 structure on the μm to nm scales was commonly observed in all studies, where the B2 matrix is Al-Co-Ni rich, while the A2 inclusions are Co-Cr-Fe rich. Morphologically, the A2 inclusions appear on three quite well-separated length scales,[16] (*i*) coarse (average size 1–5 μm), conveniently denoted as generation 1 (A2 gen-1), (*ii*) medium-scale A2 gen-2 (50–150 nm), and (*iii*) fine-scale A2 gen-3 (<10 nm). In addition, there is an A2 shell of a few nm thickness around the A2 gen-1 and A2 gen-2 inclusions at the A2–B2 interfaces, the composition of which is CoFe rich but contains almost no Al and Cr. The complex magnetism of this highly structurally and chemically heterogeneous system was investigated at a fixed temperature $T = 300$ K in a spatially resolved manner with nanometric resolution by the transmission electron microscopy (TEM) methods of Fresnel mode of Lorentz TEM and off-axis electron holography.[16] It was reported that the Al-Co-Ni-rich B2 matrix is weakly ferromagnetic (FM), while all three generations of the Co-Cr-Fe-rich A2 inclusions are strongly FM. The strongest FM contribution was identified to come from the thin CoFe-rich A2 shells around the A2 gen-1 and A2 gen-2 inclusions. The magnetic interactions between the A2 core-shell FM particles and the weakly FM Al-Co-Ni-rich B2 matrix could not be determined by the local TEM methods, so the bulk magnetism of the Al-Co-Cr-Fe-Ni HEA system remains unexplored.

In this paper, we complement the previously reported TEM-detected spatially resolved local magnetism at $T = 300$ K of the $AlCo_{0.5}Cr_{0.5}FeNi$ (equivalent to $Al_{25}Co_{12.5}Cr_{12.5}Fe_{25}Ni_{25}$, in at.%) polygrain HEA[16] with a study of the bulk magnetism in a broad temperature interval from 2 to 400 K that has developed in the $Al_{28}Co_{20}Cr_{11}Fe_{15}Ni_{26}$ single-crystalline HEA, prepared by the Czochralski method. A different synthesis route of our material and its different chemical composition have resulted in a slightly simpler decomposition into the B2 + A2 phases as compared to that reported by Lan et al.,[16] yet the material shows a clear nanostructured morphology with spherical-like A2 nanoparticles of quite uniform size with the average diameter of 64 nm, embedded in the B2 matrix.

## Material description and characterization

We were using a Czochralski monocrystal of average composition $Al_{28}Co_{20}Cr_{11}Fe_{15}Ni_{26}$ (in at.%), with the growth details given in the STAR Methods section. This was the same material as that employed in the previous TEM study of microstructure and dislocations in mechanically deformed samples.[14] In the following, we use an abbreviated notation of the material as ACCFN. The X-ray diffraction (XRD) pattern shown in Figure S1 and the electron diffraction data presented in Feuerbacher[14] confirm that the material is composed of two phases, the B2 matrix and the A2 inclusions, where the unit cell parameter of both phases is $a = 2.875$ Å. High-resolution scanning transmission electron microscopy (STEM) images have shown that, in all crystal directions, the lattice planes of the inclusions are perfectly congruent with those of the matrix so that the lattices of the B2 and A2 phases are aligned and in perfect registry.[14]

The nanostructure and the local chemical compositions were determined by bright-field (BF) STEM imaging, high-angle annular dark-field (HAADF) STEM imaging, and energy dispersive X-ray spectroscopy (EDS) point and line analysis and elemental mapping. For the STEM investigations, a lamella of about 50 nm thickness was prepared with the focused ion beam (FIB) technique using gallium ions. HAADF-STEM images on two magnification scales are shown in Figures 1A and 1B, where the nanostructured morphology of a matrix with dispersed spherical-like nanoparticles is evident. The nanoparticles' diameters $d$ are quite uniform, with the average value $\overline{d} = 64$ nm and standard deviation $\sigma_d = 10$ nm. The density of the A2 nanoparticles estimated from the HAADF-STEM images is about 6 vol %. The EDS-determined composition of the A2 nanoparticles is $Al_1Co_{18}Cr_{54}Fe_{24}Ni_3$ (in at.%). By neglecting the very small Al and Ni contents, which are within the experimental uncertainty of the EDS method, the chemical composition of the nanoparticles is $Co_{19}Cr_{56}Fe_{25}$. The composition of the B2 matrix is $Al_{27}Co_{24}Cr_4Fe_{14}Ni_{31}$, which, by neglecting the small Cr content can be written as $Al_{28}Co_{25}Fe_{15}Ni_{32}$. The B2 matrix can hence be considered roughly as Cr-free Al-Co-Fe-Ni, while the A2

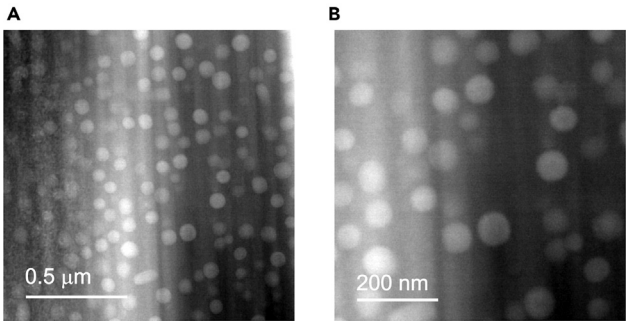


**Figure 1. HAADF-STEM images of the ACCFN HEA**
(A and B) HAADF-STEM images of the ACCFN material on two magnification scales.

nanoparticles are Cr-rich but Al- and Ni-free Co-Cr-Fe. The EDS elemental maps shown in Figure 2A and the elemental line profiles measured over the 100-nm path that crosses one nanoparticle (Figure 2B) confirm the above analysis. The distribution of the Co, Cr, and Fe elements within the nanoparticles appears quite uniform. An enrichment of the Co and Fe elements within the nanoparticles' surface layer (at the A2–B2 interfaces) of thickness about 2 nm can also be claimed (Figure 2C), indicating the same type of a core-shell structure of the A2 inclusions, as reported for the composition $AlCo_{0.5}Cr_{0.5}FeNi$.[16] The distribution of the elements in the Al-Co-Fe-Ni B2 matrix is also quite uniform.

While our TEM results indicate that the distribution of elements within the Al-Co-Fe-Ni B2 matrix and the Co-Cr-Fe A2 nanoparticles is quite homogeneous (apart from the core-shell structure of the latter), further compositional nanostructuring of the elements on the 1-nm scale within the A2 nanoparticles is likely. It has been observed before in the equiatomic AlCoCrFeNi HEA by the more sensitive method of atom probe tomography (APT).[13] The APT has confirmed that the four elements in the Al-Co-Fe-Ni B2 matrix are indeed distributed quite homogeneously on the nm scale. However, the Co-Cr-Fe A2 inclusions are further nanostructured on the 1-nm scale by decomposing into CoFe-rich and Cr-rich domains. The sizes of both types of domains are between 2 and 5 nm. Due to the difference between the magnetic properties of iron and cobalt on one side (their elemental metals are FM) and chromium (an antiferromagnet – AFM) on the other side, the magnetic states of the two types of spin clusters are different. This nanoscale decomposition makes the Co-Cr-Fe A2 inclusions to be true nanostructured magnetic objects. The extremely fine-scale spinodal decomposition into the CoFe-rich and Cr-rich phases is known to occur in the Co–Cr–Fe bulk ferromagnets[17–19] and is attributed to the miscibility gap in the Co–Cr–Fe system.[20] We did not perform an APT analysis of our material, but it is reasonable to assume that the above results also hold for our ACCFN alloy.

## RESULTS

### Magnetization versus temperature

The direct-current (dc) magnetization, measured in the temperature interval between 1.8 and 400 K for the zero-field-cooled (zfc) and field-cooled (fc) protocols in low magnetic fields $\mu_0 H =$ 0.5, 5, 10, and 100 mT, is shown in Figure 3A (experimental details are given in the STAR Methods section). An FM-type phase transition is observed at $T_C \approx$ 390 K. In the lowest magnetic field of 0.5 mT, splitting of the zfc and fc magnetizations, $M_{zfc}$ and $M_{fc}$, is observed just below $T_C$ (and expanded portion of the $M_{zfc}$ and $M_{fc}$ curves in the vicinity of $T_C$ is shown in the inset of Figure 3A). Upon cooling, the $M_{fc} - M_{zfc}$ difference is roughly constant down to about 15 K, whereas below that temperature it starts to increase strongly because $M_{zfc}$ decreases rapidly toward zero upon $T \rightarrow 0$, while $M_{fc}$ remains constant. This behavior is characteristic of nonergodic, magnetically frustrated spin systems like spin glasses, where spin fluctuations slow down on cooling and spins freeze in random directions in the absence of an external magnetic field.[21,22] In an increasing magnetic field, the bifurcation point of the $M_{zfc}$ and $M_{fc}$ is shifted continuously from $T_C$ to lower temperatures and the $M_{fc} - M_{zfc}$ difference in the $T \rightarrow 0$ limit gets smaller. For the highest applied field $\mu_0 H =$ 100 mT, there is no longer any difference between the zfc and fc magnetizations, which perfectly overlap down to the lowest temperature of 1.8 K. The observation of the $M_{fc} - M_{zfc}$ difference indicates that the spins in the investigated ACCFN material are coupled via the exchange interaction and form a kind of a collective magnetic state (with magnetic domains), very likely spatially very inhomogeneous. The external magnetic field tends to polarize the spins into the field direction via the Zeeman interaction. A relatively low field of 100 mT

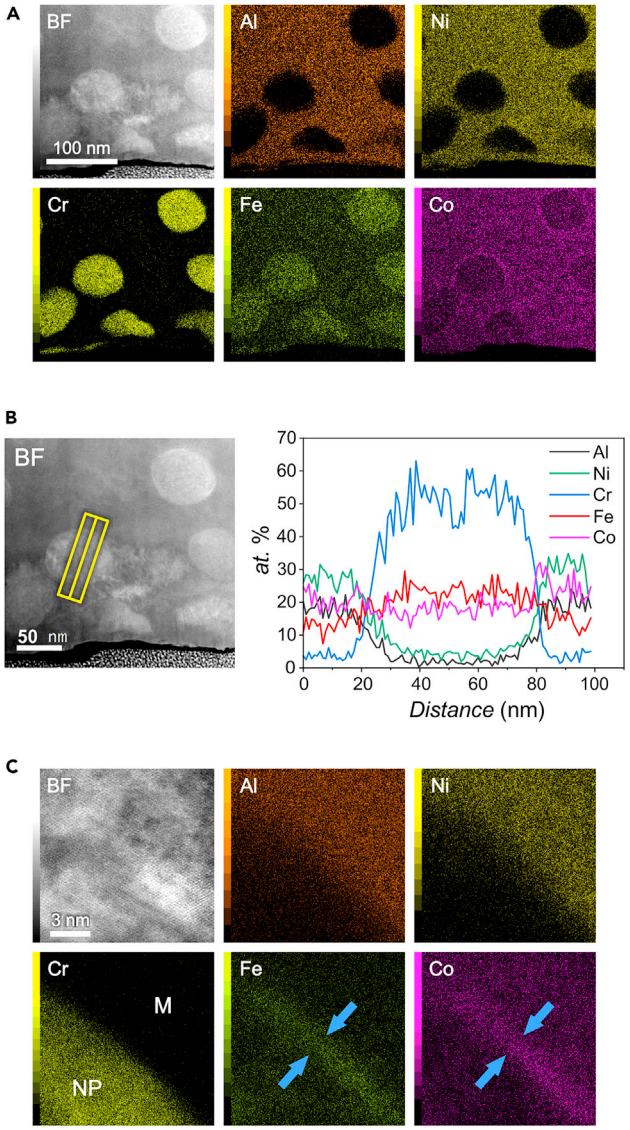


**Figure 2. STEM-EDS elemental maps and compositional line profiles of the ACCFN material**

(A) STEM-EDS elemental maps of the ACCFN material. The BF-STEM image of the investigated area is shown in the upper left panel.

(B) STEM-EDS compositional line profiles of the elements, measured along a 100-nm path that crosses one nanoparticle. The path is drawn in the BF image (left panel).

(C) STEM-EDS elemental maps of the interface region between the A2 nanoparticle and the B2 matrix. The BF-STEM image of the investigated area is shown in the upper left panel. The location of the Cr-rich nanoparticle (NP) is best identified in the chromium map, while the matrix (M) contains no Cr. An enrichment of the Co and Fe elements at the nanoparticle surface in a shell of about 2 nm thickness is visible (marked by arrows in the Co and Fe maps), confirming the core-shell structure of the nanoparticle.

is already strong enough for the Zeeman interaction to win over the exchange interaction, and the fragile internal magnetic structure is destroyed.

## Magnetization versus magnetic field

The magnetization versus the magnetic field, $M(H)$, curves were measured for the magnetic field sweep $\mu_0 H = \pm 7$ T at temperatures between 400 and 1.8 K (Figure 4A). The $M(H)$ curves are FM like, with a rapid increase in the close vicinity of $H = 0$, followed by a saturation plateau. Though the $M(H)$ curves appear to be simple FM at a first glance (where "simple" denotes a spin system with FM interactions only), there is one

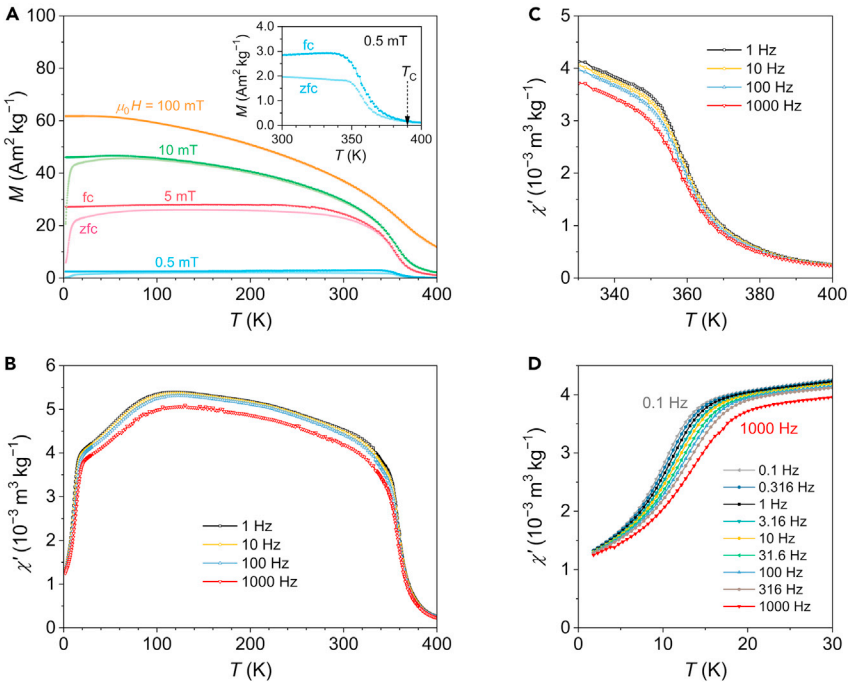


**Figure 3. Dc and ac magnetization of the ACCFN material**

(A) Temperature-dependent zero-field-cooled ($M_{zfc}$) and field-cooled ($M_{fc}$) magnetizations in magnetic fields $\mu_0 H =$ 0.5, 5, 10, and 100 mT (values indicated in the graph). The inset shows an expanded portion of the $M_{zfc}$ and $M_{fc}$ curves in the vicinity of $T_C \approx$ 390 K in the lowest magnetic field of 0.5 mT.

(B) Temperature-dependent real part of the ac susceptibility $\chi'$ at logarithmically spaced frequencies $\nu =$ 1, 10, 100, and 1000 Hz (values indicated in the graph).

(C) Frequency-dependent $\chi'$ in the high-temperature range 330–400 K around $T_C \approx$ 390 K.

(D) $\chi'$ in the low-temperature range 1.8–30 K (measured at additional frequencies, nine altogether).

detail which reveals that the actual magnetic state contains also an asperomagnetic (ASPM) component, characteristic of a heterogeneous spin system with mixed FM and AFM interactions, where the FM interactions are dominant.[23,24] In an asperomagnet, the part of the $M(H)$ curve originating from the FM spin fraction saturates to a horizontal plateau at high magnetic fields, while the part due to the AFM spin fraction is linear in the magnetic field up to the highest field. The total $M(H)$ curve, which is a sum of the FM and AFM contributions, consequently saturates at high fields to a linear, inclined line with the slope determined by the AFM susceptibility instead to a horizontal plateau.[23] The $M(H)$ curve at $T =$ 1.8 K is presented separately in Figure 4B, together with the theoretical fit assuming that the magnetization contains a major FM and a minor ASPM component. The details of the fit and the origin of the ASPM component in the total magnetization of the ACCFN HEA are discussed in the discussion section.

The temperature-dependent $M(H)$ hysteresis loops are shown in Figure 4C on an expanded field axis. The hysteresis appears already at high temperatures just below $T_C \approx$ 390 K and is then practically constant down to about 15 K, with a coercive field $\mu_0 H_c =$ 0.9 mT. Below 15 K, the hysteresis width starts to increase rapidly, reaching the coercive field value $\mu_0 H_c =$ 6.6 mT at 1.8 K. The temperature-dependent coercive field below 50 K is shown in the inset of Figure 4C.

## Alternating-current magnetic susceptibility

The alternating-current (ac) magnetic susceptibility was measured in a sinusoidal magnetic field of amplitude $\mu_0 H_0 =$ 0.05 mT at logarithmically spaced frequencies $\nu =$ 1, 10, 100, and 1000 Hz. The real part of the ac susceptibility $\chi'$ in the temperature range 1.8–400 K is shown in Figure 3B. Unlike the thermodynamic magnetic phase transitions in homogeneous media, where $\chi'$ usually shows a rather sharp, frequency-independent maximum at the transition temperature, the $\chi'$ of the ACCFN sample shows a very broad hump with the maximum at about 100 K, which is frequency dependent, $\chi'(\nu)$, in the entire temperature range below $T_C \approx$ 390 K. Such behavior is characteristic of highly inhomogeneous magnetic materials, signaling

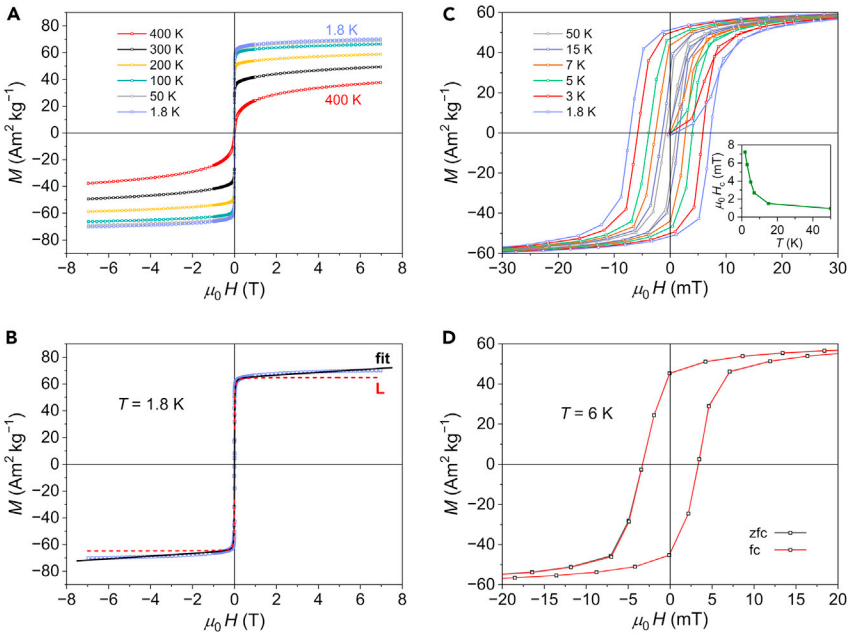


**Figure 4. Magnetization versus magnetic field curves of the ACCFN material**

(A) Magnetization versus magnetic field, $M(H)$, curves at temperatures between 400 and 1.8 K (values indicated in the graph).

(B) $M(H)$ curve at $T =$ 1.8 K with theoretical fit $M = M_{FM} + M_{AFM} = M_0\mathcal{L}(x) + \mu_0 kH$ (black solid curve), described in the text. The dashed red curve (denoted by L) shows the FM component $M_0\mathcal{L}(x)$ of the fit.

(C) Temperature-dependent $M(H)$ hysteresis loops on an expanded field axis. The inset shows the temperature-dependent coercive field below 50 K.

(D) Zfc and fc $M(H)$ curves at $T =$ 6 K zoomed on the field axis to show the hysteretic region. The sample was cooled from 400 K in zero field (the zfc protocol) and in a 7-T field (the fc protocol), and then a field sweep of $\pm$7 T was performed. The two curves are indistinguishable on the graph.

nonergodicity of at least a fraction of the spin system, where the coupled spins are unable to follow the driving ac field instantaneously.[22] The frequency-dependent $\chi'$ in the high-temperature range 330–400 K around the $T_C$ is shown in Figure 3C, while $\chi'$ in the low-temperature range 1.8–30 K (measured at additional frequencies, nine altogether) is presented in Figure 3D. The rapid decrease of $\chi'$ below 15 K upon cooling and the fact that the magnitude of $\chi'$ decreases there continuously with increasing frequency can be interpreted as a continuous freeze-out of spin fluctuations of a fraction of spins in the system, characterized by a broad distribution of fluctuation times, as typical for a nonergodic magnetically frustrated system.[22]

## zfc and fc hysteresis curves

In a highly inhomogeneous magnetic system with mixed FM and AFM exchange interactions, where the FM interactions largely dominate, there exists a possibility of formation of spatially localized FM-type magnetic clusters with very large effective magnetic moments of order 20–20,000 Bohr magnetons $\mu_B$. For interacting clusters, such state is known as a mictomagnetic state or a cluster glass,[25] whereas noninteracting clusters would form a superparamagnetic state. In a mictomagnet at sufficiently low temperatures and in zero magnetic field, the clusters freeze continuously with random orientations in a manner analogous to the spin-glass freezing, making the frustrated spin system nonergodic on the experimental observation timescale. The mictomagnetic state is best probed experimentally by performing measurements of the $M(H)$ hysteresis curves for the zfc and fc protocols. Cooled in a zero magnetic field to the measurement temperature (the zfc protocol) and then performing the field sweep, the $M(H)$ curve shows low remanence and coercivity, while cooled in a field (the fc protocol), the remanence is much larger and the hysteresis loop is shifted in the direction opposite to the magnetic field, an effect similar to the exchange bias observed in magnetic multilayer structures and magnetic nanoparticles.[25] The shift of the hysteresis loop in the fc experiment is a consequence of the collective alignment of cluster moments by the external magnetic field into a giant super-moment, which then produces the displacement field.

In order to check for the possibility of a mictomagnetic state (a cluster glass) in the ACCFN HEA, we have performed measurements of the $M(H)$ curves for the zfc and fc protocols, by cooling the sample from 400 K either in zero field or in a 7-T field to the measurement temperature $T = 6$ K and then performing the field sweep of $\pm 7$ T. The zfc and fc $M(H)$ curves, zoomed on the field axis to show clearly the hysteretic region, are displayed in Figure 4D. The two curves perfectly overlap, with no change in the hysteresis width and no shift on the field axis of the fc curve with respect to the zfc one. This result excludes the possibility of a mictomagnetic state in the ACCFN HEA, despite its highly inhomogeneous structure and concentrated amounts of the magnetic elements Co, Cr, Fe, and Ni.

### Thermoremanent magnetization time decay

Remanent magnetization is the magnetization that persists in a magnetic material after the external magnetic field is removed. For the characterization of inhomogeneous collective magnetic states, a convenient quantity is the thermoremanent magnetization (TRM), which is obtained by continuously cooling the spin system in a magnetic field $H_{fc}$ from the paramagnetic phase to the measurement temperature $T_m$ somewhere within the collective state, where the cooling is stopped and the spin system is let to age isothermally in $H_{fc}$ for a "waiting" (aging) time $t_w$ of the order of minutes to hours. After $t_w$, the field is suddenly cut to zero and the TRM time decay is monitored for macroscopic times up to several hours. The magnitude of the TRM and the speed of its time decay generally depend on the measurement temperature $T_m$, the cooling field $H_{fc}$ (which should be low enough not to destroy the internal magnetic structure), and the waiting time $t_w$, and this dependence helps to unravel the nature of the nontrivial collective spin state. In magnetically frustrated systems (spin glasses, geometrically frustrated spin lattices, magnetic nanoparticles, …), the TRM time decay is logarithmically slow, by further slowing down with decreasing $T_m$ and increasing $t_w$, while the TRM amplitude increases with decreasing $T_m$ and decreases with increasing $H_{fc}$. Such behavior is interpreted as a slow approach of a nonergodic spin system toward thermal equilibrium with zero magnetization, but the equilibrium can never be reached on the experimental timescale due to the broad distribution of spin fluctuation times that extend over many orders of magnitude.[26–33] For a ferromagnet with substantial coercivity, the TRM is practically frozen (constant) in time and its time decay is unobservable in this type of experiment because the spin order within the FM domains is rigid due to strong coupling of the spins, while reorientations of the domains with large effective magnetic moments via thermal fluctuations to demagnetize the material are unlikely to happen.

The TRM-decay experiments in the ACCFN HEA were performed by always starting the continuous cooling run at 400 K (in the paramagnetic phase) through $T_C$ to different measurement temperatures $T_m$ between 200 and 5 K. The chosen magnetic field $\mu_0 H_c = 0.5$ mT was low enough to ensure preservation of the fragile internal magnetic structure. At each $T_m$, the aging time of $t_w = 1$ h was employed prior to cutting the field to zero (which was accomplished in about 10 s) and the TRM decay was then monitored for a time of 3 h. The resulting TRM decays, normalized to the magnetization value just before cutting the field to zero, $M_{TRM}(t)/M_{fc}$, are shown on a logarithmic timescale in Figure 5A, where the following observations are evident. The TRM amplitude $M_{TRM}(0)/M_{fc}$ increases upon lowering the $T_m$ continuously in the entire investigated temperature range, where the increase becomes particularly strong below 15 K. In the "high-temperature" range $T_m > 15$ K, the TRM practically does not decay with time (it is constant) within the observation time window of 3 h. In the "low-temperature" range $T_m < 15$ K, a weak TRM decay is clearly observable (see the curves at $T_m = 8$, 7, and 6 K in Figure 5A), where the decay further slows down upon lowering the $T_m$ and becomes again almost unobservable at $T_m = 5$ K. This indicates that, below 15 K, there is a (presumably small) fraction of spins in the ACCFN material that behave more like spin glass and their respective TRM part is decaying faster with time after $H_{fc} \rightarrow 0$, in addition to the majority spin fraction whose TRM part is FM-like and remains frozen (constant in time) during the observation time window of 3 h. The origin of the two types of spin fractions will be discussed in the discussion section.

## DISCUSSION

We first discuss the difference between the disordered FM state and the ASPM state, both of which coexist in the investigated ACCFN material. The Al-Co-Cr-Fe-Ni HEA is a magnetically concentrated system, with a distribution of four different types of 3*d* magnetic moments on the lattice sites. In the electrically conducting environment, the moments are coupled via the indirect exchange interaction. The Co, Fe, and Ni elements are FM as elemental metals, suggesting that the pairs of like neighbors (Co–Co, Fe–Fe, and Ni–Ni) in the Al-Co-Cr-Fe-Ni HEA show preference for a parallel (FM) spin alignment. The Cr elemental metal, on the other hand, is

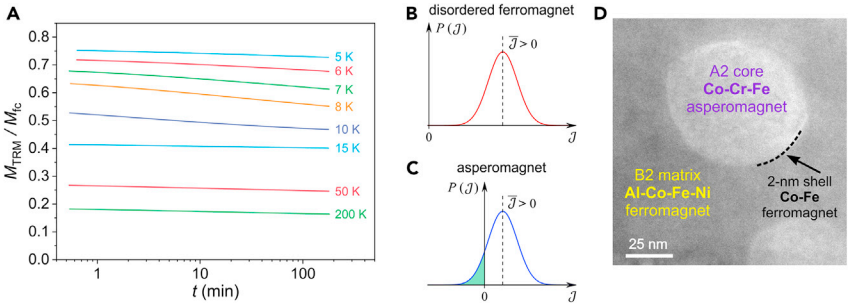


**Figure 5. Thermoremanent magnetization of the ACCFN material and schematic distributions of the exchange-coupling constants**

(A) Thermoremanent magnetization (TRM) time-decay curves at different measurement temperatures $T_m$ between 200 and 5 K (values indicated in the graph). Cooling was performed in a magnetic field $\mu_0 H_c = 0.5$ mT, and the aging time of $t_w = 1$ h was employed at each $T_m$ prior to cutting the field to zero.

(B and C) Schematic presentation of the distribution function of the exchange coupling constants $P(\mathcal{J})$ for a disordered ferromagnet and an asperomagnet (the AFM part of the distribution is colored green).

(D) BF-STEM image of the ACCFN material, indicating schematically the ferromagnetic Al-Co-Fe-Ni B2 matrix, the asperomagnetic core of the Co-Cr-Fe A2 nanoparticle, and the thin ferromagnetic CoFe-rich nanoparticle shell.

antiferromagnetic, so that the spins of the Cr–Cr like pairs align antiparallel (AFM). *Ab initio* calculations for the Cantor alloy CoCrFeMnNi have predicted that the pairs of unlike FM neighbors Co–Fe, Co–Ni, and Fe–Ni also favor parallel (FM) spin alignment, while the unlike pairs of Cr with the Co, Fe, and Ni have the spins aligned antiparallel (AFM).[34–38] Adopting those results to our ACCFN material, the Cr-free B2 matrix with composition $Al_{28}Co_{25}Fe_{15}Ni_{32}$ represents a system with FM interactions only, while the Cr-rich A2 nanoparticles of composition $Co_{19}Cr_{56}Fe_{25}$ possess mixed FM and AFM interactions.

In a topologically distorted and chemically disordered HEA lattice, there is an enormous number of different local chemical environments and bond lengths, resulting in continuous distributions of the exchange interactions $P(\mathcal{J})$, magnetic anisotropy $P(D)$, and dipolar magnetic fields $P(H_d)$. For chemically disordered alloys containing 3*d* magnetic moments, it is well established that random local magnetic anisotropy is generally too weak to pin the magnetization direction at the atomic scale.[23] Such alloys are exchange dominated, where the type of magnetic ordering is predominantly determined by the type of the $P(\mathcal{J})$ distribution. It is reasonable to assume that $P(\mathcal{J})$ can be modeled as a continuous and symmetric bell-like distribution in the $\mathcal{J}$-space. For a system with FM interactions only, the $P(\mathcal{J})$ distribution extends entirely on the positive $\mathcal{J}>0$ axis (Figure 5B), which defines the disordered FM state.[23] In such a state, there is a multitude of FM-ordered spin domains of different sizes with distributed effective magnetic moments. In contrast, for a system with mixed FM/AFM interactions, where the FM interactions are dominant, the $P(\mathcal{J})$ distribution extends on both $\mathcal{J}>0$ (FM coupling) and $\mathcal{J}<0$ (AFM coupling) sides of the $\mathcal{J}$ axis, but the average exchange interaction is biased toward a net positive value, $\overline{\mathcal{J}}>0$ (Figure 5C). This is by definition an ASPM state,[23] in which there exists a distribution of spatially localized FM and AFM spin domains, with the FM ones in majority.

Since out of the four magnetic elements present in the ACCFN material, the Al-Co-Fe-Ni B2 matrix (of the volume fraction about 94%) contains only the three FM elements Co, Fe, and Ni, it is straightforward to consider that it is FM, constituting the disordered FM state that undergoes the FM transition at $T_C \approx$ 390 K. The Co-Cr-Fe A2 nanoparticles (of about 6% vol. fraction), on the other hand, contain the AFM element Cr and the two FM elements Co and Fe so that the interspin interactions are mixed FM/AFM. In view of the core-shell structure of the nanoparticles, the thin CoFe-rich shells of about 2 nm thickness are FM, while the Co-Cr-Fe nanoparticle cores are ASPM. This is indicated schematically in the BF-STEM image shown in Figure 5D.

Considering the total magnetization of the ACCFN material at low temperatures, it contains a large FM component originating from the B2 matrix, the A2 nanoparticle shells, and the FM fraction of the ASPM state developed within the A2 nanoparticle cores, while the AFM fraction of the ASPM state gives riseto a tiny AFM component in the total magnetization. This kind of structure of the total magnetization is best observed experimentally in the low-temperature $M(H)$ curves, which can be written as a sum

$M = M_{FM} + M_{AFM} = M_0\mathcal{L}(x) + \mu_0 kH$. The FM part of the magnetization can be conveniently modeled by the Langevin function $\mathcal{L}(x) = \coth x - 1/x$ with $x = \mu_0\mu H/k_BT$ (and $M_0$ is the saturation magnetization), which reproduces the overall $M(H)$ dependence well but cannot account for the hysteresis. The Langevin model assumes that the group magnetic moment $\mu$ is a classical vector that can assume any value ($\mu \rightarrow \infty$), accounting for the large effective magnetic moments of the FM clusters. For large $x$ (obtained for large $\mu$ and/or low temperature $T$), the $\mathcal{L}(x \rightarrow \infty)$ saturates to a horizontal plateau. The AFM part of the magnetization is linear in $H$ up to the highest field, and the slope of the linear $M(H)$ line is determined by the AFM susceptibility $\mu_0 k$. At large magnetic fields $H$, the total magnetization $M = M_{FM} + M_{AFM}$ consequently saturates to a linear behavior due to the presence of the AFM component.

The above model was used to fit the $M(H)$ curve at $T = 1.8$ K, shown in Figure 4B. A reasonable fit (solid black curve, denoted by "fit") was obtained with the fit parameters $M_0 = 65$ $Am^2kg^{-1}$, $\mu = (520 \pm 40)$ $\mu_B$ and $k = (0.98 \pm 0.17)$ $Am^2kg^{-1}T^{-1}$. The FM component of the fit only, $M_0\mathcal{L}(x)$, is shown by a dashed red curve (denoted by L, standing for Langevin), demonstrating that the experimental data saturate to a linear behavior in the high-field regime. This confirms the existence of a small AFM component in the total magnetization (and hence the ASPM state) in the ACCFN HEA. Here, the analysis of the $M(H)$ curve measured at the lowest temperature of 1.8 K is essential because the Langevin function of the FM component then saturates to a horizontal plateau already at a relatively small $x$ value and the linear behavior observed for magnetic fields $\mu_0 H \geq 1.5$ T is determined solely by the AFM magnetization component.

ASPM spin ordering is known in the context of amorphous magnets.[24] Asperomagnets are considered to be a subclass of a broad class of spin glasses that encompass a wide range of magnetically diluted and concentrated systems, randomly site-disordered crystalline or amorphous materials, and site-ordered but geometrically frustrated spin lattices.[21] Spin glasses are generally frustrated spin systems because no spin configuration can satisfy all bonds and minimize the energy at the same time. Frustration results in an ergodicity break below a certain "spin-freezing" temperature $T_f$, where at $T<T_f$ the spin system is no more in the thermodynamic limit, but the experimentally observable physical quantities become time dependent, determined by the observation time window of the employed experimental technique.[21,22] Ergodicity breaking is a consequence of a very broad spectrum of spin fluctuation times that extend from microscopic up to macroscopic times, such as days or years (depending on the temperature). Typical experimentally observable broken-ergodicity phenomena below $T_f$ in frustrated spin systems are (*i*) a continuously growing difference between the fc and zfc dc magnetizations upon cooling, where $M_{fc}$ is constant below $T_f$, while $M_{zfc}$ decreases toward zero, (*ii*) a frequency-dependent ac susceptibility $\chi'(\nu)$, and (*iii*) remanence of the spin system, with logarithmically slow time decay of the thermoremanent magnetization.[26–33] The above broken-ergodicity phenomena have indeed been observed in the ACCFN HEA below 15 K in the temperature-dependent $M_{zfc}$ and $M_{fc}$ dc magnetizations (Figure 3A), the $M(H)$ hysteresis curves (Figure 4C), the low-temperature ac susceptibility (Figure 3D), and the TRM time decays (Figure 5A), confirming that the ASPM state in the ACCFN HEA is magnetically frustrated and undergoes an ergodic-nonergodic spin-freezing transition at $T_f \approx 15$ K. The ASPM state develops below $T_f$ inside the A2 nanoparticle cores, owing to their nanostructured character (small spin domains, as described in the chapter on material description and characterization) with mixed AFM/FM competing interactions. The nanoparticle shells are very likely FM already at higher temperatures, but it is not possible to claim this unambiguously from the present experiments because their contribution to the total FM magnetization is masked by the much stronger FM contribution from the B2 matrix. The disordered FM state of the B2 matrix is not frustrated and remains ergodic in the entire investigated temperature range (the measured physical quantities do not depend on the experimental time window of the employed measurement technique), owing to the much larger FM-ordered spin domains that are stable against thermal reorientations.

## Conclusions

The investigated $Al_{28}Co_{20}Cr_{11}Fe_{15}Ni_{26}$ single-crystalline HEA is a nanostructured magnetic material, consisting of A2 nanoparticles of rather uniform size with an average diameter of 64 nm, chemical composition $Co_{19}Cr_{56}Fe_{25}$, and about 6% volume fraction, embedded in a B2 matrix of composition $Al_{28}Co_{25}Fe_{15}Ni_{32}$ with about 94% volume fraction. Quite generally, the nanoparticles start showing size-specific physical properties that are different from those of a bulk material at diameters typically below about 20 nm.[12] The A2 nanoparticle sizes in the ACCFN material are just at the boundary between a nanomaterial and a

bulk material, but due to further clustering of the elements on the nm scale within the nanoparticles, they behave as true nanomagnetic objects.

The decomposition of the material into two structural entities, the B2 matrix and the A2 nanoparticles that both contain magnetic 3*d* elements, raises the question whether the magnetic state of the ACCFN HEA can be described as a single collective spin state, where the spins of the two entities are strongly coupled across the B2–A2 boundaries, or the magnetic state should be considered as an inhomogeneous mixture of two different, more or less independent states. For a single collective state, the magnetic state of the B2 matrix would influence the magnetic ordering within the nanoparticles (and vice versa), whereas in the case of an inhomogeneous mixture of the magnetic states, the magnetic order within each structural entity would develop independently, without significant "cross talk" to the other entity. The analysis of our results efficiently explains the formation of the FM state in the matrix and the ASPM state in the nanoparticles by considering predominantly the chemical composition and the type of magnetic 3*d* elements (FM or AFM) present in each entity, which is equivalent to treating the formation of the two states independent from each other. Consequently, the bulk magnetic state of the ACCFN HEA is best described as a spatially inhomogeneous mixture of the disordered FM state of the B2 matrix and the ASPM state of the A2 nanoparticles that are more or less independent from each other. The ASPM order in the nanoparticles is magnetically frustrated, resembling a spin glass, while the FM order in the matrix is of conventional type for disordered ferromagnets.

### Limitations of the study

Our TEM EDS elemental mapping has identified and confirmed the core-shell structure of the A2 nanoparticles. Magnetic measurements have revealed that the nanoparticle cores with composition Co-Cr-Fe order asperomagnetically, which follows the expectations due to the presence of two FM elements (Co and Fe) and one antiferromagnetic element (Cr). The nanoparticle shells are strongly enriched in the two ferromagnetic elements Co and Fe, so they are expected to be ferromagnetic. This could not be verified experimentally by the employed bulk magnetization measurement methods due to the presence of a much stronger FM signal from the B2 Al-Co-Fe-Ni matrix.

## STAR★METHODS

Detailed methods are provided in the online version of this paper and include the following:

- KEY RESOURCES TABLE
- RESOURCE AVAILABILITY
  - Lead contact
  - Materials availability
  - Data and code availability
- EXPERIMENTAL MODEL AND STUDY PARTICIPANT DETAILS
- METHOD DETAILS
  - Synthesis of the material
  - XRD and TEM EDS characterization
  - Magnetic measurements
- QUANTIFICATION AND STATISTICAL ANALYSIS

## SUPPLEMENTAL INFORMATION

Supplemental information can be found online at https://doi.org/10.1016/j.isci.2023.106894.

## ACKNOWLEDGMENTS

The Slovenian authors acknowledge financial support from the Slovenian Research Agency (research core funding No. P1-0125).

## AUTHOR CONTRIBUTIONS

Conceptualization of the work was done by M.F. and J.D. The material was grown by M.F., while the samples for measurements were prepared by J.L. XRD experiment was performed by A.M., whereas A.J. and G.D. performed electron microscopy imaging and EDS elemental mapping data acquisition and analysis. P.K. and S.V. have performed magnetic data acquisition and analysis. J.D. has performed data

interpretation and wrote original draft manuscript, whereas review and editing of the manuscript were done by P.K., M.W. and M.F. All authors discussed the results and commented on the manuscript.

## DECLARATION OF INTERESTS

The authors declare no competing interests.

## INCLUSION AND DIVERSITY

We support inclusive, diverse, and equitable conduct of research.

Received: February 9, 2023
Revised: May 1, 2023
Accepted: May 12, 2023
Published: May 18, 2023

## REFERENCES

1. Zhang, Y. (2019). High-Entropy Materials: A Brief Introduction (Springer), pp. 1–33.

2. Feuerbacher, M., Heidelmann, M., and Thomas, C. (2014). Hexagonal high-entropy alloys. Mater. Res. Lett. *3*, 1–6.

3. Takeuchi, A., Amiya, K., Wada, T., Yubuta, K., and Zhang, W. (2014). High-entropy alloys with a hexagonal close-packed structure designed by equi-atomic alloy strategy and binary phase diagrams. JOM *66*, 1984–1992.

4. Lužnik, J., Koželj, P., Vrtnik, S., Jelen, A., Jagličić, Z., Meden, A., Feuerbacher, M., and Dolinšek, J. (2015). Complex magnetism of Ho-Dy-Y-Gd-Tb hexagonal high-entropy alloy. Phys. Rev. B *92*, 224201.

5. Vrtnik, S., Lužnik, J., Koželj, P., Jelen, A., Luzar, J., Jagličić, Z., Meden, A., Feuerbacher, M., and Dolinšek, J. (2018). Disordered ferromagnetic state in the Ce-Gd-Tb-Dy-Ho hexagonal high-entropy alloy. J. Alloys Compd. *742*, 877–886.

6. Vrtnik, S., Lužnik, J., Koželj, P., Jelen, A., Luzar, J., Krnel, M., Jagličić, Z., Meden, A., Feuerbacher, M., and Dolinšek, J. (2019). Magnetic phase diagram and magnetoresistance of Gd-Tb-Dy-Ho-Lu hexagonal high-entropy alloy. Intermetallics *105*, 163–172.

7. Krnel, M., Vrtnik, S., Jelen, A., Koželj, P., Jagličić, Z., Meden, A., Feuerbacher, M., and Dolinšek, J. (2020). Speromagnetism and asperomagnetism as the ground states of the Tb-Dy-Ho-Er-Tm "ideal" high-entropy alloy. Intermetallics *117*, 106680.

8. Jelen, A., Jang, J.H., Oh, J., Kim, H.J., Meden, A., Vrtnik, S., Feuerbacher, M., and Dolinšek, J. (2021). Nanostructure and local polymorphism in "ideal-like" rare-earths-based high-entropy alloys. Mater. Char. *172*, 110837.

9. Cantor, B., Chang, I.T.H., Knight, P., and Vincent, A.J.B. (2004). Microstructural development in equiatomic multicomponent alloys. Mater. Sci. Eng. *375–377*, 213–218.

10. Luzar, J., Priputen, P., Drienovský, M., Vrtnik, S., Koželj, P., Jelen, A., Wencka, M., Gačnik, D., Mihor, P., Ambrožič, B., et al. (2022). Zero-magnetostriction magnetically soft high-entropy alloys in the $AlCoFeNiCu_x$ ($x$ = 0.6–3.0) system for supersilent applications. Adv. Mater. Interfac. *9*, 2201535.

11. See, e.g. Murthy, B.S., Yeh, J.-W., and Ranganathan, S. (2014). High-Entropy Alloys (Elsevier).

12. Coey, J.M.D. (2010). Magnetism and Magnetic Materials (Cambridge University Press), pp. 264–304.

13. Manzoni, A., Daoud, H., Völkl, R., Glatzel, U., and Wanderka, N. (2013). Phase separation in equiatomic AlCoCrFeNi high-entropy alloy. Ultramicroscopy *132*, 212–215.

14. Feuerbacher, M. (2016). Dislocations and deformation microstructure in a B2-ordered $Al_{28}Co_{20}Cr_{11}Fe_{15}Ni_{26}$ high-entropy alloy. Sci. Rep. *6*, 29700.

15. Chaudhary, V., Gwalani, B., Soni, V., Ramanujan, R.V., and Banerjee, R. (2018). Influence of Cr substitution and temperature on hierarchical phase decomposition in the AlCoFeNi high entropy alloy. Sci. Rep. *8*, 15578.

16. Lan, Q., Kovács, A., Caron, J., Du, H., Song, D., Dasari, S., Gwalani, B., Chaudhary, V., Ramanujan, R.V., Banerjee, R., and Dunin-Borkowski, R.E. (2022). Highly complex magnetic behavior resulting from hierarchical phase separation in AlCo(Cr)FeNi high-entropy alloys. iScience *25*, 104047.

17. Okada, M., Thomas, G., Homma, M., and Kaneko, H. (1978). Microstructure and magnetic properties of Fe–Cr–Co alloys. IEEE Trans. Magn. What Mag. *14*, 245–252.

18. Jin, S., and Chin, G. (1987). Fe-Cr-Co magnets. IEEE Trans. Magn. What Mag. *23*, 3187–3192.

19. Xiang, Z., Zhang, L., Xin, Y., An, B., Niu, R., Mardani, M., Siegrist, T., Lu, J., Goddard, R.E., Man, T., et al. (2021). Ultrafine microstructure and hardness in Fe-Cr-Co alloy induced by spinodal decomposition under magnetic field. Mater. Des. *199*, 109383.

20. Kaneko, H., Homma, M., Nakamura, K., Okada, M., and Thomas, G. (1977). Phase diagram of Fe–Cr–Co permanent magnet system. IEEE Trans. Mag. What Mag. *13*, 1325–1327.

21. Binder, K., and Young, A.P. (1986). Spin glasses: experimental facts, theoretical concepts, and open questions. Rev. Mod. Phys. *58*, 801–976. and references therein.

22. Mydosh, J.A. (1993). Spin Glasses: An Experimental Introduction (Taylor & Francis), p. 67.

23. Coey, J.M.D. (2010). Magnetism and Magnetic Materials (Cambridge University Press), pp. 209–218.

24. O'Handley, R.C. (1999). Modern Magnetic Materials: Principles and Applications (Wiley)), pp. 391–410.

25. Mydosh, J.A. (1993). Spin Glasses: An Experimental Introduction (Taylor & Francis), pp. 32–34.

26. Bouchaud, J.-P., Cugliandolo, L.F., Kurchan, J., and Mézard, M. (1998). Out of equilibrium dynamics in spin-glasses and other glassy systems. In Spin Glasses and Random Fields, A.P. Young, ed. (World Scientific)), pp. 161–224.

27. Kawashima, N., and Rieger, H. (2004). Recent progress in spin glasses. In Frustrated Spin Systems, H.T. Diep, ed. (World Scientific)), pp. 491–596.

28. Vincent, E., Hammann, J., Ocio, M., Bouchaud, J.-P., and Cugliandolo, L.F. (1997). Slow dynamics and aging in spin glasses. In Complex Behaviour of Glassy Systems, Lecture Notes in Physics 492, M. Rubí and C. Pérez-Vicente, eds. (Springer), pp. 184–219.

29. Nordblad, P., and Svedlindh, P. (1998). Experiments on spin glasses. In Spin Glasses and Random Fields, A.P. Young, ed. (World Scientific)), pp. 1–28.

30. Bouchaud, J.-P., Dupuis, V., Hammann, J., and Vincent, E. (2001). Separation of time and length scales in spin glasses: temperature as a microscope. Phys. Rev. B *65*, 024439.

31. Lederman, M., Orbach, R., Hammann, J.M., Ocio, M., and Vincent, E. (1991). Dynamics in spin glasses. Phys. Rev. B *44*, 7403–7412.

32. Chu, D., Kenning, G.G., and Orbach, R. (1995). Effect of magnetic fields on the relaxation of the thermoremanent magnetization in spin glasses. Phil. Mag. B *71*, 479–488.

33. Dolinšek, J., Slanovec, J., Jagličić, Z., Heggen, M., Balanetskyy, S., Feuerbacher, M., and Urban, K. (2008). Broken ergodicity, memory effect, and rejuvenation in Taylor-phase and decagonal Al3(Mn,Pd,Fe) complex intermetallics. Phys. Rev. B *88*, 064430.

34. Schneeweiss, O., Friák, M., Dudová, M., Holec, D., Šob, M., Kriegner, D., Holý, V., Beran, P., George, E.P., Neugebauer, J., and Dlouhý, A. (2017). Magnetic properties of the CrMnFeCoNi high-entropy alloy. Phys. Rev. B *96*, 014437.

35. Zhang, Y., Zuo, T., Cheng, Y., and Liaw, P.K. (2013). High-entropy alloys with high saturation magnetization, electrical resistivity and malleability. Sci. Rep. *3*, 1455.

36. Tian, F., Varga, L.K., Chen, N., Delczeg, L., and Vitos, L. (2013). *Ab initio* investigation of high-entropy alloys of 3*d* elements. Phys. Rev. B *87*, 075144.

37. Ma, D., Grabowski, B., Körmann, F., Neugebauer, J., and Raabe, D. (2015). *Ab initio* thermodynamics of the CoCrFeMnNi high entropy alloy: importance of entropy contributions beyond the configurational one. Acta Mater. *100*, 90–97.

38. Dong, Z., Schönecker, S., Li, W., Chen, D., and Vitos, L. (2018). Thermal spin fluctuations in CoCrFeMnNi high entropy alloy. Sci. Rep. *8*, 12211.

39. Beleggia, M., De Graef, M., and Millev, Y. (2006). Demagnetization factors of the general ellipsoid: an alternative to the Maxwell approach. Philos. Mag. A *86*, 2451–2466.

## STAR★METHODS

### KEY RESOURCES TABLE

| REAGENT or RESOURCE | SOURCE | IDENTIFIER |
|---|---|---|
| Chemicals, peptides, and recombinant proteins | | |
| Aluminum rod, 6N | Mateck | B03HP500 |
| Cobalt 3N5 | Johnson Matthey<br>Alfa Aesar | 635115<br>010454 |
| Chromium 5N | Keppels | - |
| Iron 4N pieces | Chempur | 902379 |
| Nickel 4N5 rod | MRC | 20-101GNI00001000 |
| 4N5 wire | Alfa Aesar | 10928 |

### RESOURCE AVAILABILITY

#### Lead contact

Further information and requests for resources should be directed to and will be fulfilled by the Lead Contact, Janez Dolinšek (jani.dolinsek@ijs.si).

#### Materials availability

The study did not generate new unique reagents. All chemicals were obtained from commercial resources and used as received.

#### Data and code availability

- The published article includes all datasets generated or analyzed during this study.
- All data reported in this paper will be shared by the lead contact upon request.
- This paper does not report original code.
- Any additional information required to reanalyze the data reported in this work paper is available from the lead contact upon request.

### EXPERIMENTAL MODEL AND STUDY PARTICIPANT DETAILS

Our study does not use experimental models typical in the life sciences.

### METHOD DETAILS

#### Synthesis of the material

The material was synthesized by first producing an ingot of average composition $Al_{28}Co_{20}Cr_{11}Fe_{15}Ni_{26}$ (in at.%) in a high-frequency levitation furnace, which was then used as a melt for the Czochralski monocrystal growth from a heterogeneous tungsten seed under 650 mbar Ar atmosphere at a pulling rate of 1 mm/h. Due to the near-equilibrium nature of the Czochralski method (the crystal is inherently thermally annealed for several hours during slow pulling), the material was well equilibrated. The crystal consisted of several grains of an average volume about 1 $mm^3$.

#### XRD and TEM EDS characterization

The XRD diffraction pattern was recorded using PANalytical X'Pert PRO MPD X-ray powder diffractometer equipped with a primary monochromator, delivering pure Cu $K\alpha_1$ radiation ($\lambda$ = 1.54056 Å) and a 128-channel position-sensitive silicon multi-strip detector.

The HAADF-STEM images, EDS elemental maps and elemental concentration line profiles were obtained by a Cs-corrected Jeol ARM 200 CF STEM microscope equipped with an SDD Jeol Centurio

energy-dispersive X-ray spectrometer. The operating voltage was set to 200 kV. The lamella for the STEM investigations was prepared by the FIB Helios NanoLab NL650 FEI dual-beam system using gallium ions.

### Magnetic measurements

Magnetic measurements were conducted on a Quantum Design MPMS3 SQUID magnetometer equipped with a 7-T magnet, operating at temperatures between 1.8 and 400 K. The TRM experiments were performed with the copper AC/ULF coil in the MPMS3 magnetometer to ensure the highest level of repeatability and accuracy. A needle-like sample of approximate dimensions 0.4 × 0.8 × 5.5 $mm^3$ was used in the magnetic measurements, with the long dimension aligned along the magnetic field to reduce the demagnetization effects. In the measurement of the $M(H)$ isothermal magnetization loops presented in Figure 4, two corrections were applied: (*i*) a correction for the remanent field of the superconducting magnet that was performed by measuring a pure Pd sample with the same measurement sequence and (*ii*) a correction for the demagnetizing field, so that the horizontal axis on the graphs represents the internal magnetic field $H$ in the material and not the externally applied field $H_a$ (using $H = H_a - \mathcal{N}M$, where $\mathcal{N}$ is the demagnetizing tensor). The principal components $\mathcal{N}_a$, $\mathcal{N}_b$, and $\mathcal{N}_c$ of the demagnetizing tensor for a general ellipsoid with major axes $a$, $b$, $c$ (where $c$ is the longest axis) were calculated from Equations 16–20 of,[39] where the $\mathcal{N}_{a,b,c}$ values depend only on the ratios $\tau_a = c/a$ and $\tau_b = c/b$.

Since $\mathcal{N}_a$ and $\mathcal{N}_b$ are obtained from $\mathcal{N}_c$ by a proper rotation of the $\tau_a$ and $\tau_b$ parameters, we give here only the value $\mathcal{N}_c = 0.02$.

## QUANTIFICATION AND STATISTICAL ANALYSIS

The mean value and standard deviation of the nanoparticles' diameters given in the material description and characterization section were determined by a statistical analysis of 200 nanoparticles visible in the HAADF-STEM image of Figure 1A. The EDS-determined chemical composition of the A2 nanoparticles is a mean value measured over 20 nanoparticles, while the EDS composition of the B2 matrix is a mean value measured over a set of 20 randomly spaced points in the matrix. All elemental concentrations were rounded to the closest integers.